6202 *Biochemistry* **2009,** *48,* 6202–6212
DOI: 10.1021/bi9005754

BIOCHEMISTRY
including biophysical chemistry & molecular biology
Article

Small Molecules Bound to Unique Sites in the Target Protein Binding Cleft of Calcium-Bound S100B As Characterized by Nuclear Magnetic Resonance and X-ray Crystallography[†]

Thomas H. Charpentier,[‡] Paul T. Wilder,[‡] Melissa A. Liriano,[‡] Kristen M. Varney,[‡] Shijun Zhong,[§] Andrew Coop,[§] Edwin Pozharski,[§] Alexander D. MacKerell, Jr.,[§] Eric A. Toth,*[,‡] and David J. Weber*[,‡]

[‡]*Department of Biochemistry and Molecular Biology, The University of Maryland School of Medicine, 108 North Greene Street, Baltimore, Maryland 21201, and* [§]*Department of Pharmaceutical Sciences, The University of Maryland School of Pharmacy, 20 Penn Street, Baltimore, Maryland 21201*

Received April 3, 2009; Revised Manuscript Received May 22, 2009

ABSTRACT: Structural studies are part of a rational drug design program aimed at inhibiting the S100B−p53 interaction and restoring wild-type p53 function in malignant melanoma. To this end, structures of three compounds (SBi132, SBi1279, and SBi523) bound to Ca^{2+}-S100B were determined by X-ray crystallography at 2.10 Å (R_{free} = 0.257), 1.98 Å (R_{free} = 0.281), and 1.90 Å (R_{free} = 0.228) resolution, respectively. Upon comparison, SBi132, SBi279, and SBi523 were found to bind in distinct locations and orientations within the hydrophobic target binding pocket of Ca^{2+}-S100B with minimal structural changes observed for the protein upon complex formation with each compound. Specifically, SBi132 binds nearby residues in loop 2 (His-42, Phe-43, and Leu-44) and helix 4 (Phe-76, Met-79, Ile-80, Ala-83, Cys-84, Phe-87, and Phe-88), whereas SBi523 interacts with a separate site defined by residues within loop 2 (Ser-41, His-42, Phe-43, Leu-44, Glu-45, and Glu-46) and one residue on helix 4 (Phe-87). The SBi279 binding site on Ca^{2+}-S100B overlaps the SBi132 and SBi523 sites and contacts residues in both loop 2 (Ser-41, His-42, Phe-43, Leu-44, and Glu-45) and helix 4 (Ile-80, Ala-83, Cys-84, Phe-87, and Phe-88). NMR data, including saturation transfer difference (STD) and ^{15}N backbone and ^{13}C side chain chemical shift perturbations, were consistent with the X-ray crystal structures and demonstrated the relevance of all three small molecule−S100B complexes in solution. The discovery that SBi132, SBi279, and SBi523 bind to proximal sites on Ca^{2+}-S100B could be useful for the development of a new class of molecule(s) that interacts with one or more of these binding sites simultaneously, thereby yielding novel tight binding inhibitors specific for blocking protein−protein interactions involving S100B.

There are more than 20 S100 proteins originally named because of their solubility in 100% saturated ammonium sulfate (*1*). Like calmodulin (CaM) and most other EF-hand-containing proteins, S100 proteins typically function as a calcium-activated switch that binds and regulates the biological function of numerous protein targets (Figure 1) (*2*−*8*). Members of the S100 protein family are distributed in a cell-specific manner (*9*−*11*), including in a large number of human cancers (*12*−*14*). S100B protein levels are elevated in malignant melanoma (*14*), anaplastic astrocytomas (*15*, *16*), and glioblastomas (*17*). In the case of malignant melanoma, high concentrations of S100B correlate directly with poor prognosis in patients (*18*−*20*), and therefore, S100B levels are used as a clinical marker for melanoma as well as for other cancers.

In mechanistic studies, S100B was found to bind directly to the p53 tumor suppressor protein in primary human malignant melanoma cells, reduce p53 protein levels, and inhibit wild-type p53 functions (*21*−*26*). Therefore, elevated levels of S100B may contribute to cancer progression by downregulating wild-type p53 protein (*26*). Correspondingly, p53 protein levels and its associated activities were restored in malignant melanoma when S100B expression was inhibited by siRNA (*25*). With these $siRNA^{S100B}$ results in mind, a rational drug design approach was initiated to develop small molecule inhibitors that bind Ca^{2+}-S100B, prevent formation of the S100B−p53 complex, and restore p53-dependent tumor suppressor activity in cancer (*27*−*29*). Previously, a model for drug binding based on NMR and X-ray crystallography of one such molecule, pentamidine (Pnt), bound to Ca^{2+}- and Ca^{2+}, Zn^{2+}-bound S100B was reported (*30*). As observed in these X-ray crystal structures, Pnt was found to bind to the target protein

[†]This work was supported by National Institutes of Health Grants GM58888 (D.J.W.) and CA107331 (D.J.W.) and American Cancer Society Grant CDD107745 (D.J.W.).

*To whom correspondence should be addressed. D.J.W.: Department of Biochemistry and Molecular Biology, The University of Maryland School of Medicine, 108 N. Greene St., Baltimore, MD 21201; phone, (410) 706-4354; fax, (410) 706-0458; e-mail, dweber@umaryland.edu. E.A.T.: Department of Biochemistry and Molecular Biology, The University of Maryland School of Medicine, 108 N. Greene St., Baltimore, MD 21201; phone, (410) 706-5345; fax, (410) 706-8297; e-mail, etoth001@umaryland.edu.

 Published on Web 05/26/2009

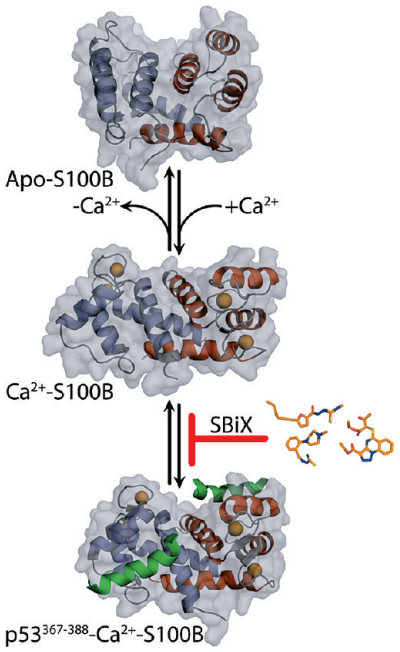

FIGURE 1: "Calcium switch" in S100B. Shown are ribbon and surface diagrams of apo-S100B (NMR, PDB entry 1B4C), Ca^{2+}-bound S100B (X-ray, PDB entry 1MHO), and $p53^{367-388}$-bound Ca^{2+}-S100B (NMR, PDB entry 1DT7) illustrating the calcium-dependent reorientation in each S100B subunit. The helices in each S100B subunit are colored red and blue with the loop regions colored gray. The two calcium ions per subunit are represented as orange spheres. This calcium-dependent conformational change is required for S100B to interact with the C-terminal regulatory region of $p53^{367-388}$. S100B inhibitors (SBi*X*) bind to the p53 binding site and inhibit formation of the S100B−p53 complex.

binding pocket as well as to another well-defined site near the dimer interface. Here we report three additional small molecule−S100B complexes and demonstrate that additional small molecule binding sites exist that are in the proximity of the Pnt binding sites. These data could be used for the rational design of a new high-affinity inhibitor of S100B, which could have clinical benefits for treating cancers with elevated levels of S100B such as malignant melanoma and astrocytomas.

EXPERIMENTAL PROCEDURES

Materials. All chemicals and reagents were ACS-grade or higher and typically purchased from Sigma-Aldrich unless otherwise indicated. SBi*X* molecules were purchased from Maybridge (Maybridge numbers, SBi132,[1] KM09613; SBi279, SEW05759; SBi523, HTS12452). $^{15}NH_4Cl$ and ^{13}C-labeled glucose were purchased from Cambridge Isotope Laboratories (Andover, MA). All buffers were passed through Chelex-100 resin to remove trace metals prior to use.

Bacterial Expression and Purification of Wild-Type S100B. Recombinant S100B protein (rat and bovine) was expressed in *Escherichia coli* [HMS174(DE3) strain] and purified as previously described (*31*). Yields of S100B protein were typically 20−30 mg of purified protein per liter of bacterial culture. For NMR experiments, S100B protein was prepared using defined medium that included ^{15}N-labeled NH_4Cl as the only nitrogen source and ^{13}C-labeled glucose as the sole carbon source (*31*).

NMR Spectroscopy. Purified ^{15}N-labeled S100B and ^{13}C- and ^{15}N-labeled S100B were dialyzed against 0.1 mM Tes (pH 7.2) and 0.05 mM DTT, lyophilized, hydrated in a small aliquot of ddH_2O, and stored at −80 or −20 °C. The Ca^{2+}-loaded S100B-SBi*X* NMR sample was prepared in a manner similar to that previously described (*27*) and contained 0.1−0.5 mM S100B subunit, 0−1.6 mM SBi132, 0−1.6 mM SBi523, or 0−5.0 mM SBi279, 0.34 mM NaN_3, 15 mM NaCl, 0−5% DMSO-d_6, 10 mM $CaCl_2$, 10% D_2O, and 10 mM Tes or Tris D_{11} buffer, adjusted to pH 7.2 with HCl. These chemical shift assignments were then used as a starting point during titrations with SBi*X* molecules to assign the two-dimensional (2D) $^1H-^{15}N$ and $^1H-^{13}C$ HSQC spectra of S100B (*32*, *33*). Heteronuclear single-quantum coherence (HSQC) NMR data were collected at 37 °C with a Bruker Avance III 600 (600.13 MHz for protons) or an Avance 800 US2 (800.27 MHz for protons) instrument. Both NMR spectrometers were equipped with pulsed-field gradients, four frequency channels, and triple-resonance, *z*-axis gradient cryogenic probes (*32*). Data were processed with NMRPipe (*34*), and proton chemical shifts were reported with respect to the H_2O or HDO signal taken as 4.658 ppm relative to external TSP (0.0 ppm). The ^{15}N chemical shifts were indirectly referenced as previously described using the following ratio of the zero-point frequency: 0.10132905 for ^{15}N to ^1H (*35*−*37*).

Group epitope mapping via saturation transfer difference (STD) NMR was completed for SBi*X*−S100B complexes in a manner similar to that described previously (*38*). Specifically, during the 2 s presaturation pulse, the on-resonance irradiation of the protein was performed at a chemical shift of −0.4 ppm and the off-resonance irradiation was applied at 30 ppm, where no protein signals were present. As a control, the STD experiments were conducted in the absence of a $T_{1\rho}$ filter, and as expected, the one-dimensional (1D) spectrum of holo-S100B was fully restored. The final sample contained 50 μM S100B, 0.5 mM SBi132, 2.0 mM SBi279, or 1.0 mM SBi523, 10 mM $CaCl_2$, 5% DMSO-d_6, 99.98% D_2O, 15 mM NaCl, 0.34 mM NaN_3, and 10 mM Tris D_{11} (pH 7.2). The STD data were collected at 25 °C to achieve more efficient saturation of the protein. Proton assignments of SBi132, SBi279, and SBi523 were confirmed under the conditions described above in the absence and presence of S100B using 2D TOCSY experiments (*39*).

Protein Crystallization. Bovine S100B protein was dialyzed into buffer [0.1 mM TES (pH 7.2) and 0.05 mM DTT], lyophilized, dissolved in ddH_2O to a concentration of 80−100 mg/mL (~8−10 mM subunit concentration), and stored frozen. We obtained diffraction quality crystals for the SBi523−Ca^{2+}-S100B complex by sitting drop vapor diffusion at 22 °C by mixing 2 μL of S100B protein and SBi523 small molecule [40 mg/mL S100B, 4.0 mM SBi523, 7.5 mM $CaCl_2$, and 20 mM Bis-Tris buffer (pH 6.0)] with 2 μL of reservoir solution [12.5 mM $CaCl_2$, 0.1 M Bis-Tris

[1]Abbreviations: SBi132, S100B Inhibitor 132 {2-[(5-hex-1-ynyl-2-furyl)carbonyl]-*N*-methylhydrazine-1-carbothioamide}; SBi279, S100B Inhibitor 279 (2-{[2-(4-methylpiperazino)phenyl]methylene}hydrazine-1-carbothioamide); SBi523, S100B Inhibitor 523 (ethyl-5-{[1-(ethoxycarbonyl)-2-oxopropyl]sulfanyl}[1,2,3]triazolo[1,5-*a*]quinazoline-3-carboxylate); PNT, pentamidine; DTT, dithiothreitol; TPPI, time-proportional phase incrimination; TSP, 3-(trimethylsilyl)propionic acid-d_4, sodium salt; PEG, polyethylene glycol; MME, monomethyl ether; HSQC, heteronuclear single-quantum coherence; STD, saturation transfer difference; EDTA, ethylenediaminetetraacetic acid; Tes, 2-{2-hydroxyl-1,1-[bis(hydroxymethyl)ethyl]amino}ethanesulfonic acid; Bis-Tris, 2,2-bis(hydroxymethyl)-2,2′,2″-nitrilotriethanol; Tris-HCl, tris(hydroxymethyl)aminomethane hydrochloride; DMSO, dimethyl sulfoxide; ddH_2O, deionized and doubly distilled H_2O; PDB, Protein Data Bank.

Table 1: SBi*X* Crystal and Refinement Statistics

	SBi132−Ca^{2+}-S100B[a]	SBi279−Ca^{2+}-S100B[a]	SBi523−Ca^{2+}-S100B[a]
Diffraction Statistics			
space group	$C222_1$	$C222_1$	$C222_1$
cell dimensions *a*, *b*, *c* (Å)	34.7, 90.8, 59.0	34.2, 91.2, 58.7	34.5, 89.5, 59.2
cell angles α, *β*, *γ* (deg)	90, 90, 90	90, 90, 90	90, 90, 90
resolution (Å)	45.41−2.10 (2.16−2.10)	45.60−1.98 (2.04−1.98)	44.77−1.90 (1.90−1.95)
no. of unique reflections	5321 (358)	5993 (285)	6719 (317)
completeness (%)	97.69 (88.81)	94.21 (59.88)	93.57 (60.85)
R_{sym}[b]	0.042 (0.277)	0.049 (0.233)	0.037 (0.273)
average I/σ	37.48 (4.1)	27.8 (4.1)	44.18 (3.1)
multiplicity	6.4 (3.8)	6.3 (3.8)	6.3 (3.6)
Refinement Statistics			
R_{crys}[c] (%)	20.8 (27.7)	22.9 (32.1)	21.0 (22.6)
R_{free}[c] (%)	25.7 (29.1)	28.1 (48.6)	22.8 (34.3)
no. of protein atoms	710	710	727
no. of water molecules	37	33	42
no. of non-hydrogen atoms	773	769	797
mean *B* values (Å^2)			
overall	46.16	50.58	47.21
protein atoms	45.34	50.41	46.28
water molecules	49.88	51.13	52.47
Ca^{2+} typical EF -and	51.68	47.49	42.65
Ca^{2+}-S100B EF-hand	50.76	47.80	42.27
SBi molecule	64.13[d]	52.45[e]	64.05[f]
cacodylate molecule	65.12	64.48	
root-mean-square deviation			
bond lengths (Å)	0.014	0.006	0.015
bond angles (deg)	1.828	1.525	1.620
Ramachandran plot (%)[g]			
most favored	95.1	95.1	94.0
additionally allowed	4.9	4.9	6.0
PDB entry	3GK1	3GK2	3GK4

[a] Numbers in parentheses represent data for the last outer shell. [b] $R_{sym} = \sum_h \sum_i [|I_i(h)| - |\{I(h)\}|] / \sum_h \sum_i I_i(h)$, where $I_i(h)$ is the observed intensity and $\{I(h)\}$ is the mean intensity obtained from multiple measurements. [c] R_{crys} and $R_{free} = \sum ||F_o| - |F_c|| / \sum |F_o|$, where F_o is the observed structure factor amplitude and F_c is the calculated structure factor amplitude for the working and test sets. [d] Mean *B* values (angstroms) for SBi132 are slightly higher than the mean *B* values (48.46) for side chain atoms of S100B involved in SBi132 binding (H42, F43, L44, F76, M79, I80, A83, C84, F87, and F88). [e] Mean *B* values (angstroms) for SBi279 are slightly higher than the mean *B* values (50.72) for side chain atoms of S100B involved in SBi279 binding (S41, H42, F43, L44, E45, I80, A83, C84, F87, and F88). [f] Mean *B* values (angstroms) for SBi523 are slightly higher than the mean *B* values (46.77) for side chain atoms of S100B involved in SBi523 binding (S41, H42, F43, L44, E45, E46, and F87). [g] For SBi279−Ca^{2+}-S100B and SBi132−Ca^{2+}-S100B complexes, the calculations had 78 residues in the most favored region and four residues in additionally allowed regions. For the SBi523−Ca^{2+}-S100B complex, the calculations had 79 residues in the most favored region and five residues in additionally allowed regions.

(pH 6.0), 35% PEGMME550, and 2.5% glycerol] and equilibrating for 2−3 days. After crystals formed, they were cryoprotected in a harvest solution [5.0 mM SBi1523, 15 mM $CaCl_2$, 0.1 M Bis-Tris buffer (pH 6.0), 35% PEGMME350, and 7.5% glycerol] for 30−60 s and then flash-cooled in liquid nitrogen. The SBi132−Ca^{2+}-S100B and SBi279−Ca^{2+}-S100B complexes were crystallized in a similar manner using complex-specific protein buffers [SBi132−Ca^{2+}-S100B, 40 mg/mL S100B, 7.5 mM $CaCl_2$, 4.0 mM SBi132, and 20 mM cacodylate buffer (pH 7.2); SBi279−Ca^{2+}-S100B, 40 mg/mL S100B, 7.5 mM $CaCl_2$, 4.0 mM SBi279, and 20 mM cacodylate buffer (pH 7.2)], reservoir solutions [SBi132−Ca^{2+}-S100B, 7.5 mM $CaCl_2$, 0.1 M cacodylate buffer (pH 6.5), and 28% PEG3350; SBi279−Ca^{2+}-S100B, 7.5 mM $CaCl_2$, 0.1 M cacodylate buffer (pH 6.8), and 28% PEG3350], and harvest solutions [SBi132−Ca^{2+}-S100B, 15 mM $CaCl_2$, 5.0 mM SBi132, 0.1 M cacodylate buffer (pH 6.5), 30% PEG3350, and 5% glycerol; SBi279−Ca^{2+}-S100B, 15 mM $CaCl_2$, 10 mM SBi279, 0.1 M cacodylate buffer (pH 6.8), 30% PEG3350, and 5% glycerol]. Space groups and unit cell parameters are given in Table 1. Each of the above crystal forms had one S100B subunit in the asymmetric unit.

X-ray Data Collection, Model Building, and Refinement. X-ray data for the SBi*X*−Ca^{2+}-S100B crystals were collected remotely at Stanford Synchrotron Radiation Laboratory (Menlo Park, CA) (beamlines 9-1 and 7-1) using an ADSC Quantum-315R CCD detector (Area Detector Systems Corp.). The reflection intensities were integrated and scaled with the HKL2000 suite of computer programs (*40*). The crystals of SBi132−Ca^{2+}-S100B, SBi279−Ca^{2+}-S100B, and SBi523−Ca^{2+}-S100B complexes diffracted to 2.10, 1.98, and 1.90 Å resolution, respectively. Preliminary phases were obtained via molecular replacement techniques using the structure of Ca^{2+}-bound S100B [PDB entry 1MHO (*41*)] as a search model and the computer program Phaser and molrep from the CCP4 program suite (*42*). Model building and refinement of S100B were completed using COOT and REFMAC5 (*43*, *44*). The locations of the SBi*X* molecules and several water molecules were determined by visual inspection of electron density maps calculated with $2mF_o-DF_c$ and mF_o-DF_c coefficients with COOT (*44*). The occupancy was set to 1.0 for SBi132 except for the hexyne atoms that were set to 0.5 occupancy because these atoms reside on a crystallographic 2-fold axis. For both SBi279 and SBi523,

the occupancies were set to 0.5 because these molecules reside on a crystallographic 2-fold axis. The stereochemistry was checked with WHATCHECK and PROCHEK (*45*, *46*). The quaternary structure and accessible surface areas were analyzed using the PISA server (http://www.ebi.ac.uk/msd-srv/prot_int/cgi-bin/piserver). The coordinates for the SBi132−Ca^{2+}-S100B, SBi279−Ca^{2+}-S100B, and SBi523−Ca^{2+}-S100B X-ray structures were deposited in the Protein Data Bank (*47*, *48*) and assigned the following accession numbers: 3GK1 for SBi132−Ca^{2+}-S100B, 3GK2 for SBi279−Ca^{2+}-S100B, and 3GK4 for SBi523−Ca^{2+}-S100B. Figures were generated with PyMol (http://www.pymol.org).

RESULTS

The binding of S100B to p53 downregulates tumor suppressor activity in cancer cells such as malignant melanoma (*25*, *49*), so a search for small molecules that bind S100B and prevent formation of the S100B−p53 complex was undertaken (*27*, *29*). Atomic structures of S100B in the Ca^{2+}- and p53 peptide-bound states together with computer-aided drug design, NMR, and high-throughput screening approaches were used to identify small molecules that bind S100B and inhibit the S100B−p53 interaction (*27*−*29*). Several additional S100B inhibitors were more recently discovered (S. Zhong, P. T. Wilder, D. J. Weber, and A. D. MacKerell, Jr., manuscript in preparation), including SBi132, SBi279, and SBi523, and these three molecules were examined here bound to Ca^{2+}-S100B using structural biology techniques (i.e., NMR and X-ray crytallography).

NMR Studies of S100B Inhibitors (SBiXs) and $p53^{367-388}$ *Binding to* Ca^{2+}*-S100B.* Perturbations of backbone $^{1}H-^{15}N$ heteronuclear single-quantum coherence (HSQC) correlations determined previously (*50*) and perturbations of methyl $^{1}H-^{13}C$ HSQC correlations measured here (M7, V13, I36, V56, T59, L60, M79, and V80) confirmed that the $p53^{367-388}$ peptide binds into a hydrophobic pocket on S100B that is only present in the Ca^{2+}-bound state (Figures 1 and 2A). This hydrophobic peptide binding site is well-defined in the solution NMR structure of the S100B−p53 peptide complex and includes residues from helix 1 (residues E2−R20), loop 2 (termed the hinge region, residues E39−Q50), and helix 4 (residues F70−E86) of S100B (Figures 1 and 2A) (*22*). It was this target protein binding site that was originally targeted with the goal of inhibiting the S100B−p53 interaction (*27*, *28*, *30*). Subsequently, we have identified several additional small molecules that interact with Ca^{2+}-S100B at or nearby the $p53^{367-388}$ peptide binding site (S. Zhong, P. T. Wilder, D. J. Weber, and A. D. MacKerell, Jr., manuscript in preparation).

As with the $p53^{367-388}$ peptide (Figure 2A), the binding of three small molecules (SBi132, SBi279, and SBi523) to Ca^{2+}-S100B was assessed here by monitoring perturbations of backbone $^{1}H-^{15}N$ and side chain methyl $^{1}H-^{13}C$ correlations in 2D $^{1}H-^{15}N$ and $^{1}H-^{13}C$ HSQC NMR experiments, respectively (Figure 2B−D). In HSQC titrations with SBi132 ($^{SBi132}K_D = 80 \pm 20\ \mu M$), the $^{1}H-^{15}N$ HSQC correlations of Ca^{2+}-S100B shifted [> 10 Hz (Figure 2B)] for several residues in helix 1 (A9 and F14), loop 2 (S41, F43, L44, and E51), and helix 4 (A75, V77, S78, T81, T82, C84, H85, and E86). In addition, the $^{1}H-^{13}C$ methyl HSQC correlations of Ca^{2+}-S100B shifted (> 15 Hz) for residues on helix 1 (M7, L10, and I11), helix 3 (V52 and V56), and helix 4 (M74, V77, T82) (Figure 2B, red asterisks). The binding of SBi132 to S100B was shown to be calcium-dependent since no perturbations were observed when

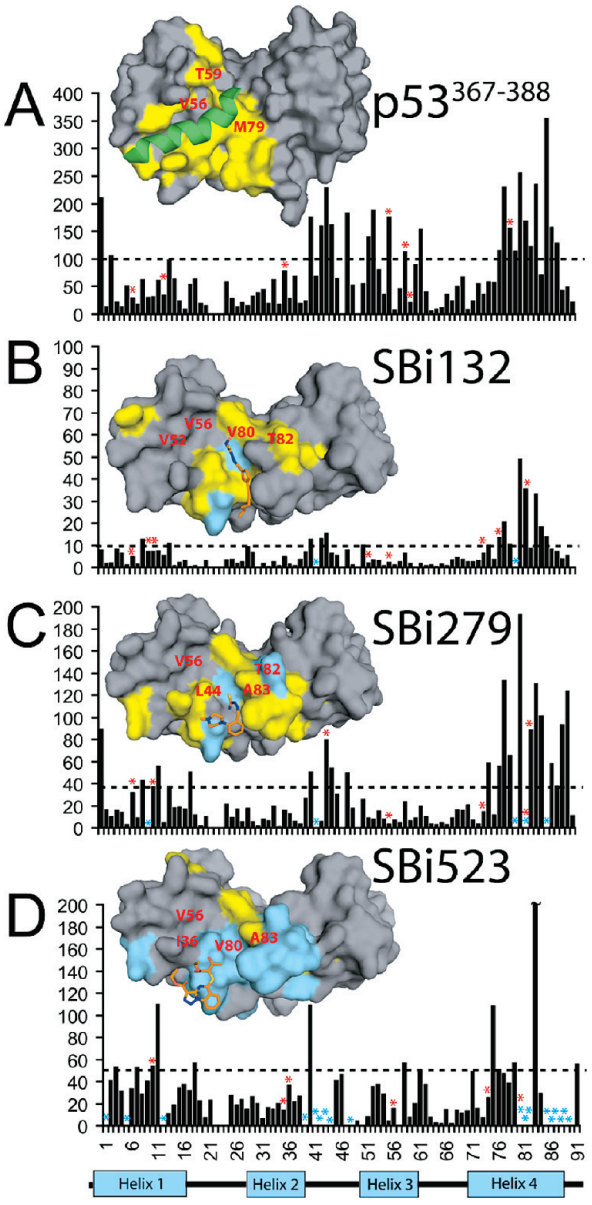

FIGURE 2: Binding of SBi*X* and $p53^{367-388}$ to Ca^{2+}-S100B as monitored by HSQC NMR titrations. Perturbations in ^{1}H and ^{15}N chemical shift values for residues above the dashed line (2 times the median of all perturbations) in S100B upon binding (A) $p53^{367-388}$, (B) SBi132 ($K_D = 0.080 \pm 0.020$ mM; specific for S100B), (C) SBi279 ($K_D = 2.0 \pm 1.0$ mM), and (D) SBi523 ($K_D = 0.120 \pm 0.03$ mM) are highlighted in yellow on the surface representation of Ca^{2+}-S100B. Residues that are chemical exchange broadened are highlighted with a cyan star in the perturbation graph and highlighted in cyan on the surface representation of Ca^{2+}-S100B. Perturbations seen in ^{1}H and ^{13}C chemical shifts are highlighted with a red star in the perturbation graph, and these specific residues found on the surface in the hydrophobic pocket are labeled in red.

SBi132 was added to apo-S100B (with EGTA). In addition, the binding of SBi132 was found to be specific for S100B since no perturbations in the $^{1}H-^{15}N$ HSQC spectrum were observed in titrations of SBi132 into ^{15}N-labeled Ca^{2+}-S100A1, the S100 protein that is most similar in sequence to that of S100B. Likewise, several of the SBi132-induced chemical shift perturbations in Ca^{2+}-S100B (Figure 2B) were similar to those observed for the binding of the $p53^{367-388}$ peptide (Figure 2A) and provided some indication that the binding sites of SBi132 and the $p53^{367-388}$ peptide could be similarly located (Figure 2A,B).

SBi279 bound Ca^{2+}-S100B significantly more weakly than SBi132 ($^{SBi279}K_D = 2.0 \pm 1.0$ mM), yet perturbations in $^1H-^{15}N$ HSQC correlations of Ca^{2+}-S100B could still be readily observed [> 35 Hz (Figure 2C)] for residues in helix 1 (A9, I11, D12, F14, and S18), loop 2 (S41, L44, E45, and K48), and helix 4 (A75, V77, S78, M79, T81, A83, C84, H85, F87, F88, E89, and H90). As for SBi132, several of the same methyl $^1H-^{13}C$ HSQC correlations of Ca^{2+}-S100B (i.e., M7, I11, V56, M74, and T82) also shifted (> 12 Hz) upon addition of SBi279, consistent with binding into the target protein binding site of Ca^{2+}-S100B. However, the binding sites for SBi132 and SBi279 were found to be somewhat different since several residues in the hinge region, including the correlation for the methyl of L44, were largely perturbed in titrations with SBi279 with little or no effect on these same residues (< 10 Hz) in titrations with SBi132 (Figure 2B,C). Another difference between SBi279 and SBi132 is that more than one-third of the residues throughout the sequence of apo-S100B shifted (> 10 Hz) upon addition of SBi279 (5.0 mM), indicative of nonspecific binding interactions occurring in the absence of calcium for this compound. Lastly, SBi279 was also found to perturb the chemical shift (> 25 Hz) of several residues in Ca^{2+}-S100A1, including residues in helix 1 (L4, A7, M8, E9, and F15), loop 2 (D46, V47, K49, D50, and A51), helix 3 (I57), loop 3 (D66), and helix 4 (V76, A79, V83, and A84). On the basis of this titration, it is possible that SBi279 has a similar binding site on Ca^{2+}-S100A1 and Ca^{2+}-S100B since several residues that were perturbed in Ca^{2+}-S100A1 align exactly in sequence with residues that shift upon binding of SBi279 to Ca^{2+}-S100B.

As with SBi132 and SBi279, the binding of SBi523 ($^{SBi523}K_D = 120 \pm 30\ \mu$M) also resulted in the perturbation of $^1H-^{15}N$ HSQC correlations (> 50 Hz; helix 1, L3, M7, L10, I11, and S18; loop 2, L40; helix 3, E58; and helix 4, A75, M79, A83, and E91) and methyl $^1H-^{13}C$ HSQC correlations (> 45 Hz; helix 1, L10; helix 2, L35 and I36; helix 3, V56; and helix 4, M74, V80, and A83) in the hydrophobic pocket of Ca^{2+}-S100B (Figure 2D). Furthermore, the HSQC correlations for several other residues in the target protein binding site of Ca^{2+}-S100B broadened and/or disappeared upon addition of SBi523 (helix 1, S1, K5, and D12; loop 2, E39, S41, H42, F43, L44, and K48; and helix 4, T81, T82, H85, E86, F87, F88, E89, and H90) (Figure 2D). As with SBi132, no perturbations were observed in titrations with apo-S100B (with EDTA), indicating that the binding of SBi523 to S100B was dependent on calcium. However, SBi523 also interacted with S100A1 in a calcium-dependent manner on the basis of chemical shift perturbations (> 10 Hz) measured by NMR (helix 1, A7, M8, E9, T10, I12, and V14; loop 1, Y26; helix 2, K34; loop 2, K49 and A51; and helix 4, F71 and A79).

As described previously for other protein−ligand complexes (*38*, *51*), saturation transfer difference (STD) NMR experiments were conducted to identify protons of SBi132, SBi279, and SBi523 that are at the SBi*X*−S100B binding interface (Figure 3). STD NMR data such as these are useful for making qualitative conclusions pertaining to the relative proximity of protons on the inhibitor to those on the protein and for epitope mapping, especially for protons or groups of protons with comparable longitudinal relaxation times (T_1) (*51*). In these studies, collection of the STD NMR data was straightforward because of the relatively low affinity of the S100B−SBi*X* complexes studied ($K_D > 50\ \mu$M) and their fast exchange kinetics (*38*). Specifically, protons from the methylhydrazine-carbothioamide group (3-proton), the aliphatic protons (4-, 5-, 6-, and 7-protons), and protons of the tetrahydrofuran ring of SBi132 were all found

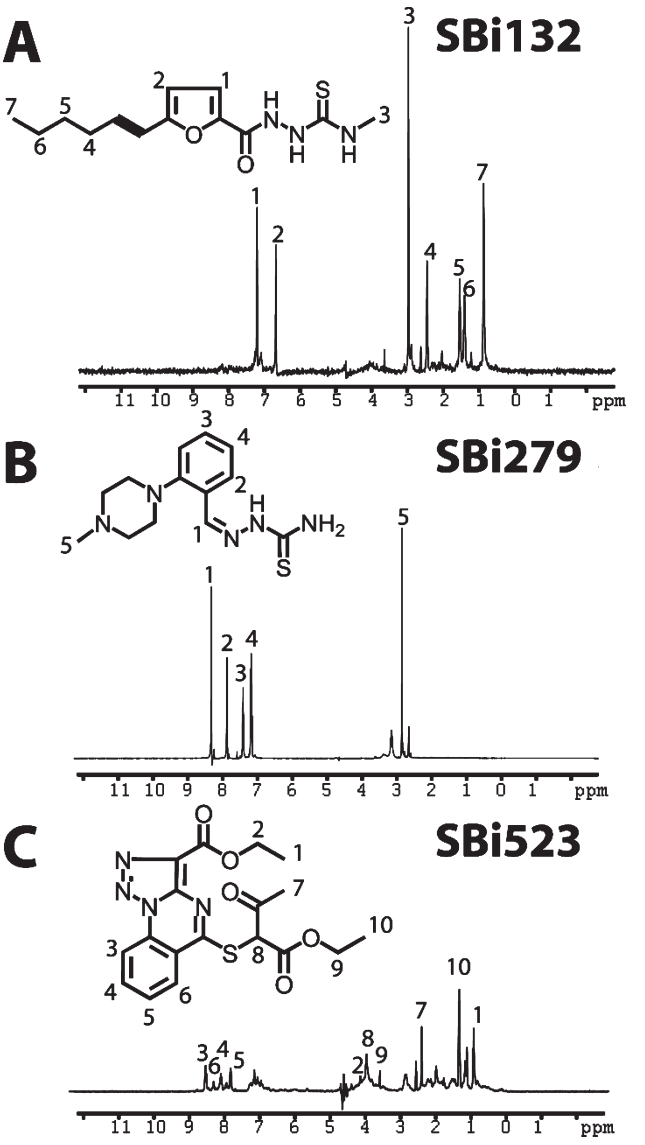

FIGURE 3: Binding of SBi*X* molecules to Ca^{2+}-S100B as monitored by STD NMR. Saturation transfer difference (STD) spectra are shown for (A) SBi132, (B) SBi279, and (C) SBi523 upon binding to Ca^{2+}-S100B.

to be proximal to Ca^{2+}-S100B as judged by their relatively strong STD signals (Figure 3A). Likewise, the benzene ring protons of SBi279 (2-, 3-, and 4-protons) were found to interact with Ca^{2+}-S100B via STD NMR, but larger STD signals were observed for methyl protons at the 5-position of the methylpiperazino group and at the alkene proton at the 1-position, indicating that the interaction with S100B is more substantial for these regions of SBi279 [1- and 5-protons (Figure 3B)]. STD NMR data were also collected for the S100B−SBi523 complex with all the protons of the compound giving rise to STD NMR data. However, the most definitive STD NMR signals were from the methyl groups (1-, 7-, and 10-protons) lining one face of the molecule and likely constitute the most buried region(s) of SBi523 in the S100B−SBi523 complex (Figure 3C). Nonetheless, the exact conformation and orientation of each SBi*X* were further characterized by X-ray crystallography to adequately define, at atomic resolution, the exact location and/or orientation of each of these small molecules in their respective S100B−SBi*X* complexes.

X-ray Structures of SBi132−, SBi279−, and SBi523−Ca^{2+}-S100B Complexes. The X-ray structures of SBi132,

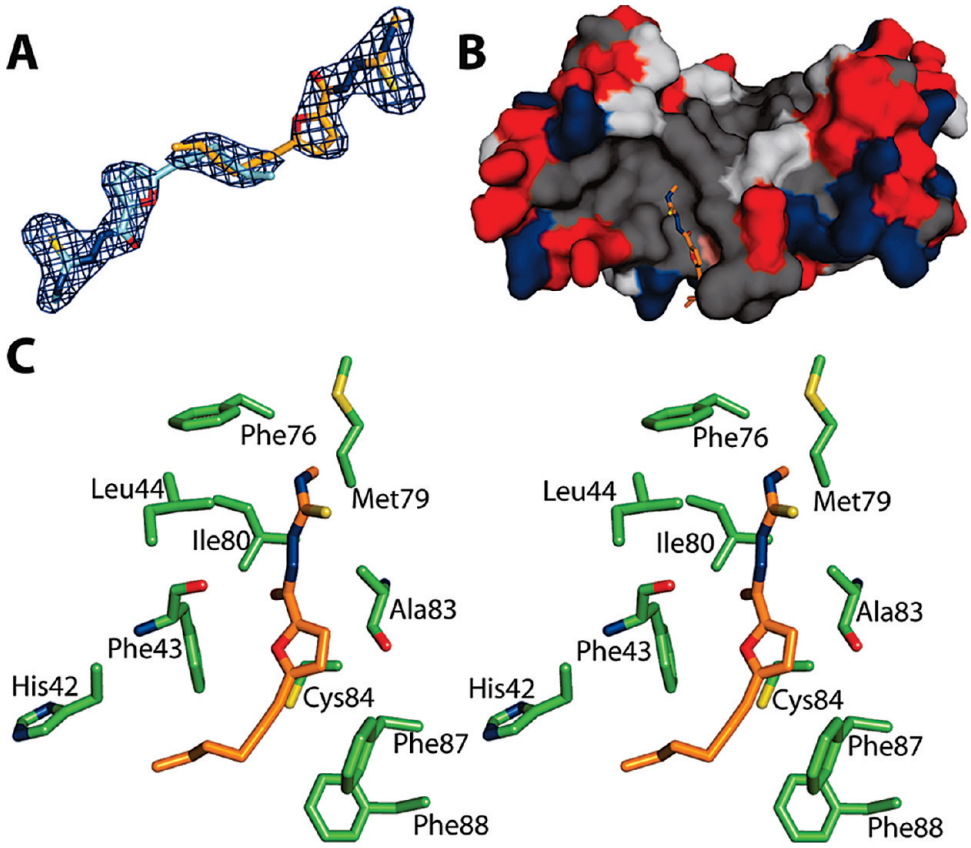

FIGURE 4: X-ray structures of the SBi132−Ca^{2+}-S100B complex. (A) Electron density maps calculated with the $2mF_o - DF_c$ coefficients (1.0σ) for SBi132. Symmetrical and overlapping orientations are shown for SBi132 molecules (orange and cyan) because of their locations at the crystallographic 2-fold axis with only a partial occupancy of 0.5 for the hexyne. (B) Surface diagram illustrating the location of the SBi132 molecule (SBi132 carbons colored gold, nitrogens blue, oxygens red, and sulfurs orange) and the polarity of the S100B surface (acidic polar, red; basic polar, blue; nonpolar, gray; neutral polar, white; cysteine, salmon). (C) Residues of S100B that are within 5 Å of SBi132 are illustrated.

SBi279, and SBi523 bound to Ca^{2+}-S100B were determined at 2.10, 1.98, and 1.90 Å resolution, respectively (Figures 4−6 and Table 1). In all three SBi*X*−Ca^{2+}-S100B structures, the asymmetric unit included a single subunit of dimeric S100B (SBi132− and SBi279−Ca^{2+}-S100B, Ser-1−Phe-88; SBi523−Ca^{2+}-S100B, Met-0−Glu-89), two calcium ions, one SBi*X* molecule, one cacolydate molecule for SBi132− and SBi279−Ca^{2+}-S100B complexes, and between 33 and 42 water molecules (Figures 4−6 and Table 1). The electron density identified for the cacodylate molecule was at the lattice interface involving residues in the pseudo-EF-hand and is likely the result of crystallization since no NMR chemical shift perturbations were observed in titrations of cacolydate (≤5 mM) to a solution of Ca^{2+}-S100B as monitored by $^{1}H-^{15}N$ HSQC experiments.

In the final refined models, residues of S100B in the SBi*X*−Ca^{2+}-S100B complexes were nearly all in the most favorable region of their respective Ramachandran plots (94−95%) with the remaining residues falling into the allowed region [5−6% (Table 1)]. The binding of the three SBi*X* compounds caused only minor structural perturbations as evidenced by low root-mean-square deviation (rmsd) values between the SBi*X*-bound structures and Ca^{2+}-S100B (PDB entry 1MHO) upon superposition (SBi132−Ca^{2+}-S100B, ^{mainchain}rmsd = 0.24 Å; SBi279−Ca^{2+}-S100B, ^{mainchain}rmsd = 0.27 Å; SBi523−Ca^{2+}-S100B, ^{mainchain}rmsd = 0.30 Å) (*31*, *41*). Furthermore, the global fold for S100B in all three SBi*X*−S100B complexes was similar to that reported for Ca^{2+}-bound S100B, Zn^{2+},Ca^{2+}-S100B (*4*, *30*), and several other Ca^{2+}-loaded S100 proteins (*2*, *3*). Specifically, each subunit of S100B in the SBi*X*−Ca^{2+}-S100B complexes contained four helices (helix 1, E2−G19; helix 2, K28−L40; helix 3, E49−D61; helix 4, D69−F88) and one small antiparallel β-sheet (strand 1, K26−K28; strand 2, D69−E67). As expected, the two EF-hand calcium binding domains in each subunit were found to coordinate two calcium ions as found previously (*52*−*54*) with the typical EF-hand of S100B in the Ca^{2+}-bound "open" conformation and the dimer interface aligned as a symmetric X-type four-helix bundle comprising helices 1 and 1′ and helices 4 and 4′, respectively (*31*, *55*, *56*) (Figure 1). Lastly, it was necessary to model the SBi*X* molecules into the electron density in two symmetrical and overlapping orientations at the lattice with each orientation having a partial occupancy (Figures 4−6). The occupancy and temperature factor for the SBi*X* molecules were constrained in each case to be identical because of their location on the crystallographic 2-fold axis.

Modeling SBi132 into the electron density maps calculated with $2mF_o - DF_c$ and $mF_o - DF_c$ coefficients showed that the SBi132 molecule was oriented in the hydrophobic pocket of Ca^{2+}-S100B with the methylhydrazine-carbothioamide moiety nearby several hydrophobic residues on the hinge (L44) and helix 4 (F76, M79, I80, A83, and C84). The hexyne moiety of SBi132 was found to be stabilized by phenylalanine residues on the hinge (F43) and further down on helix 4 (F87 and F88) as SBi132 exited the Ca^{2+}-S100B binding pocket toward solvent. Several side chains in Ca^{2+}-S100B, including those in helix 1 (K5, V13, and Q16), loop 1 (E21 and K24), loop 2 (E45), helix 3 (K55 and E58), and helix 4 (Q71 and E86), significantly changed position (rmsd > 0.8 Å) upon addition of SBi132. Several of the changes

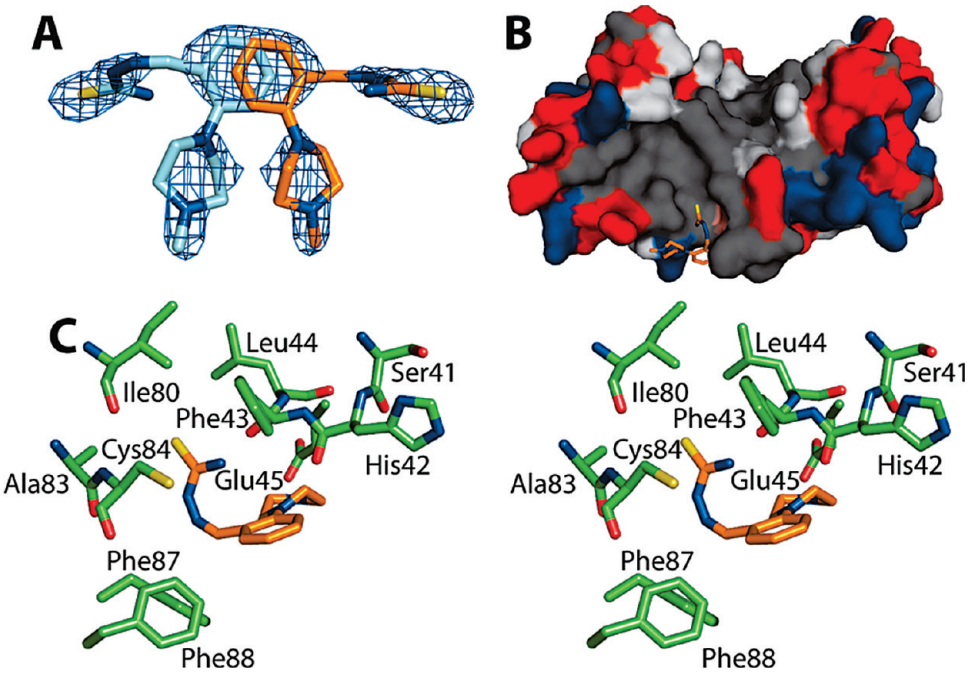

FIGURE 5: X-ray structures of the SBi279−Ca^{2+}-S100B complex. (A) Electron density maps calculated with the $2mF_o - DF_c$ coefficients (1.0σ) for SBi279. Symmetrical and overlapping orientations are shown for SBi279 molecules (orange and cyan) because of their locations at the crystallographic 2-fold axis with a partial occupancy of 0.5. (B) Surface diagram illustrating the location of the SBi279 molecule (SBi279 carbons colored orange, nitrogens blue, oxygens red, and sulfurs yellow) and the polarity of the S100B surface (acidic polar, red; basic polar, blue; nonpolar, gray; neutral polar, white; cysteine, salmon). (C) Residues of S100B that are within 5 Å of SBi279 are illustrated.

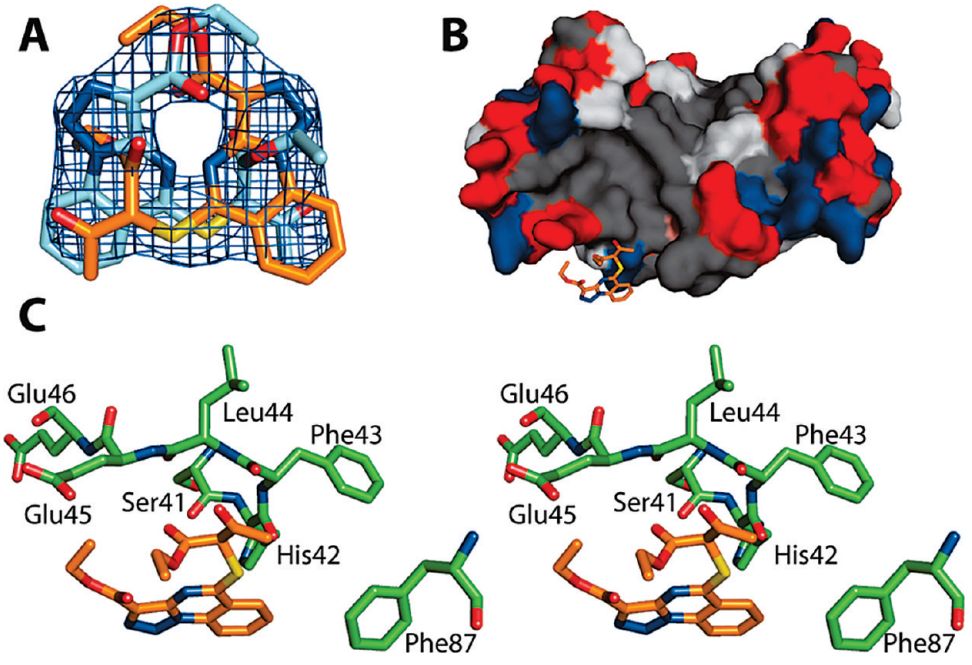

FIGURE 6: X-ray structures of the SBi523−Ca^{2+}-S100B complex. (A) Electron density maps calculated with the $2mF_o - DF_c$ coefficients (1.0σ) for SBi523. Symmetrical and overlapping orientations are shown for SBi523 molecules (orange and cyan) because of their locations at the crystallographic 2-fold axis with a partial occupancy of 0.5. (B) Surface diagram illustrating the location of the SBi523 molecule (SBi523 carbons colored orange, nitrogens blue, oxygens red, and sulfurs yellow) and the polarity of the S100B surface (acidic polar, red; basic polar, blue; nonpolar, gray; neutral polar, white; cysteine, salmon). (C) Residues of S100B that are within 5 Å of SBi523 are illustrated.

seen in helix 4 and loop 2 correspond with the interaction of the SBi132 molecule with S100B observed in the electron density maps. Overall, the S100B−SBi132 interaction was stabilized via hydrophobic interactions with residues in loop 2 (H42, F43, and L44) and helix 4 (F76, M79, I80, A83, C84, F87, and F88) contributing most to binding (Figure 4), and the structure of this S100B−SBi132 complex is fully consistent with the chemical shift perturbation and saturation transfer difference data collected in solution by NMR (Figures 2B and 3A).

The S100B−SBi279 interaction is dominated by ring−ring interactions primarily with Phe-87 and to a lesser degree with Phe-88 (Figure 5). This is unlike SBi132, which extends into a pocket defined by residues Leu-44, Phe-76, Met-79, and Ile-80. When the SBi279 and SBi132 binding sites were compared, it was

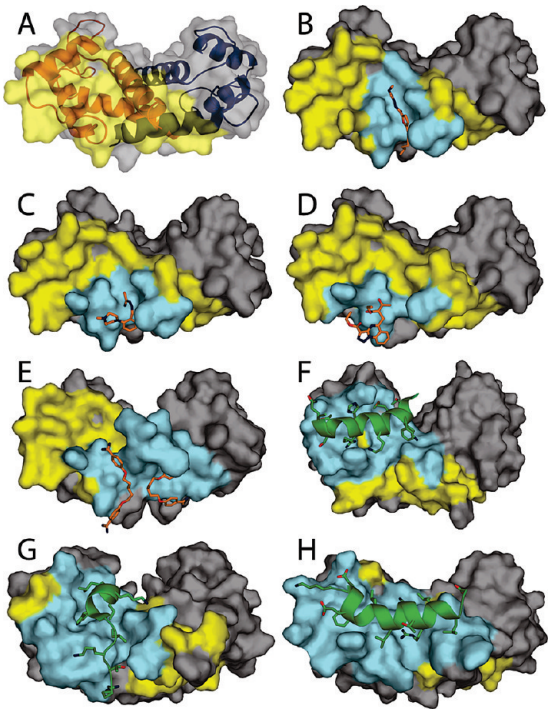

FIGURE 7: X-ray and NMR structures of peptides and small molecules bound to Ca^{2+}-S100B. (A) A surface and ribbon diagram of Ca^{2+}-S100B (X-ray, PDB entry 1MHO) is illustrated with each S100B subunit colored red and blue, respectively. Residues of Ca^{2+}-S100B that are involved in formation of a complex with either SBi1, SBi132, SBi279, SBi523, $p53^{367-388}$, TRTK12, or NDR^{62-87}, as calculated via the PISA server, are highlighted in yellow and include residues from helix 1 (V8, I11, D12, H15, and Q16), hinge/loop 2 (S41, H42, F43, L44, E45, E46, I47, K48, and E49), helix 3 (E51, V52, K55, V56, and T59), and helix 4 (F76, M79, I80/V80, T82, A83, C84, H85, E86, F87, F88, E89, and H90) (*22*, *30*, *41*, *59*, *60*). An ethylene glycol molecule was also found to bind human Ca^{2+}-S100B (nearby residues V8, I11, D12, H15, H42, F43, L44, E45, V80, A83, C84, F87, and F88), so this structure was also included when defining the S100B interaction surface [X-ray, PDB entry 2H61 (*58*)]. In panels B–H, the surface diagrams of the various SBi*X* and peptide complexes of Ca^{2+}-S100B are illustrated with residues that are involved in a specific complex shown (cyan) together with the other residues of Ca^{2+}-S100B that are involved in formation of complexes with other molecules or peptides (yellow). (B) Surface diagram of the SBi132–Ca^{2+}-S100B complex (X-ray, PDB entry 3GK1) illustrating residues of Ca^{2+}-S100B that interact with SBi132 in cyan (H42, F43, L44, F76, M79, I80, A83, C84, F87, and F88). (C) Surface diagram of the SBi279–Ca^{2+}-S100B complex (X-ray, PDB entry 3GK2) illustrating residues of Ca^{2+}-S100B that interact with SBi279 in cyan (S41, H42, F43, L44, E45, I80, A83, C84, F87, and F88). (D) Surface diagram of the SBi523–Ca^{2+}-S100B complex (X-ray, PDB entry 3GK4) illustrating residues of Ca^{2+}-S100B that interact with SBi523 in cyan (S41, H42, F43, L44, E45, E46, and F87). (E) Surface diagram of the pentamidine–Ca^{2+}-S100B complex (X-ray, PDB entry 3CR4) illustrating residues of Ca^{2+}-S100B that interact with pentamidine in cyan (V8, I11, D12, H15, Q16, H42, F43, L44, E45, C84, H85, F87, F88, and E89). (F) Surface diagram of the $p53^{367-388}$–Ca^{2+}-S100B complex (NMR, PDB entry 1DT7) illustrating residues of Ca^{2+}-S100B that interact with the p53 peptide in cyan (L44, E45, E46, I47, K48, E49, E51, V52, K55, V56, T59, F76, M79, V80, T82, A83, and E86). (G) Surface diagram of the TRTK12–Ca^{2+}-S100B complex (NMR, PDB entry 1MWN) illustrating the residues of Ca^{2+}-S100B that interact with TRTK12 in cyan (I36, H42, F43, L44, E45, E46, I47, K48, V52, K55, V56, T59, F76, M79, V80, A83, C84, E86, and F87). (H) Surface diagram of the NDR^{62-87}–Ca^{2+}-S100B complex (NMR, PDB entry 1PSB) illustrating the residues of Ca^{2+}-S100B that interact with the NDR peptide in cyan (S41, H42, F43, L44, E45, E46, I47, K48, E49, E51, V52, K55, V56, F76, M79, I80, A83, C84, E86, F87, E89, and H90).

found that SBi279 interacted with fewer residues in helix 4 (I80, A83, and C84), which could explain its lower affinity. Other residues near SBi279 include additional residues in loop 2 (S41, H42, F43, L44, and E45). As expected, several side chains change position when SBi279 binds to Ca^{2+}-S100B (rmsd > 1.0 Å), including residues in helix 1 (E2, K5, and Q16), loop 1 (E21), loop 2 (E45), helix 3 (K55), and helix 4 (Q71, E86, and F88).

In the S100B–SBi523 complex, SBi523 interacts directly with residues in loop 2 and is farther from helix 4 than found for SBi132 or SBi279 (Figures 4–6). Residues on loop 2 that contribute to SBi523 binding were found to include Ser-41, His-42, Phe-43, Leu-44, Glu-45, and Glu-46 with the only contribution observed from helix 4 being Phe-87 (Figure 6C). SBi523 is not extended like SBi132 but is arranged in a more compact conformation with hydrophobic interactions found from the three rings of the compound to hydrophobic residues on the protein. Similar to the other SBi*X* molecules, several side chains change position, including residues in helix 1 (E2, K5, V8, D12, V13, and Q16), loop 2 (E45, K48, E49, and K55), and helix 4 (Q71) in the SBi523–Ca^{2+}-S100B complex (rmsd > 0.95 Å) when compared to those of Ca^{2+}-S100B. Furthermore, a hydrogen bond was observed between the backbone carbonyl of Ser-41 and a water molecule that coordinates an oxygen atom on the ester near the sulfur group on SBi523. In addition, the backbone amide of Glu-46 coordinates with a different water molecule that, in turn, coordinates with an oxygen atom of another ester attached to the triazole ring on the symmetry mate SBi523. Thus, the combination of hydrophobic interactions and a small hydrogen bonding network in this binding site is consistent with the chemical shift perturbation data as well as binding in the micromolar range determined by NMR spectroscopy in solution.

DISCUSSION

S100B functions as a calcium-activated switch (Figure 1) that undergoes a conformational change as necessary to bind and inhibit the p53 tumor suppressor protein (*3*, *26*). Therefore, finding an inhibitor(s) that interacts specifically with S100B in the Ca^{2+}-bound state (termed SBi*X*), disrupts the S100B–p53 protein–protein interaction, and restores p53 function could be beneficial for treating cancers with elevated levels of S100B such as malignant melanoma (*25*). However, inhibiting any protein–protein interaction, including the S100B–p53 complex, represents a challenging endeavor (*57*). As a first step in achieving this goal, computer-aided drug design (CADD), high-throughput screening, and SAR by NMR approaches were completed (*28*, *29*), and several small molecule inhibitors of S100B (SBi*X*s) were identified (*27*). Applying this approach, we have identified additional inhibitors (S. Zhong et al., manuscript in preparation) and, in the work presented here, collected structural information to characterize three small molecules bound to Ca^{2+}-S100B. This information could then be used to develop higher-affinity inhibitors that bind one or more of these SBi*X* sites simultaneously and specifically inhibit the S100B–p53 protein–protein interaction.

The structures of Ca^{2+}-S100B, three S100B–peptide complexes (S100B–p53, S100B–TRTK12, and S100B–NDR kinase peptides), and two S100B–Pnt complexes (Ca^{2+}-S100B–Pnt and Zn^{2+},Ca^{2+}-S100B) were determined previously and are useful for helping to define the target protein or small molecule binding surface available on Ca^{2+}-S100B (*22*, *30*, *58–60*) (Figure 7). In comparisons of structures of apo- and Ca^{2+}-

S100B, a conformational change is observed (Figure 1), which exposes sites necessary for binding target proteins and small molecules. In fact, in one such Ca^{2+}-S100B structure (*58*), it was observed that a molecule of polyethylene glycol (PEG), which was used to promote crystallization, bound to this newly exposed hydrophobic site (Figure 7). In the three S100B−peptide structures, it was found that 25 residues define the target peptide binding sites, including one residue in helix 2 (residue 36), nine residues in the hinge region (residues 41−49), five residues in helix 3 (residues 51, 52, 55, 56, and 59), and 10 residues in helix 4 or the C-terminal loop (residues 76, 79, 80, 82−84, 86, 87, 89, and 90). In two additional structures of the inhibitor Pnt bound to Ca^{2+}- and Ca^{2+},Zn^{2+}-S100B (*27*, *30*), it was found that two Pnt molecules bind each subunit of S100B in both complexes. One Pnt molecule is located near the peptide binding site (site 1) and involves residues in the hinge (residues 42−45) and helix 4 (residues 83, 84, and 87−89). The second Pnt molecule bound outside the peptide binding site in both Ca^{2+}- and Ca^{2+},Zn^{2+}-S100B and was adjacent to a well-characterized Zn^{2+} binding site (termed site 2) (*4*, *30*). This second Pnt binding site represented an additional binding surface on S100B that was not identified in the peptide−S100B structures and was defined by residues located on helix 4 (residues 84, 85, and 87−89) as well as six additional residues in helix 1 [residues 8, 9, 11, 12, 15, and 16 (Figure 7)]. Together, these S100B structures defined a surface on S100B comprising at least 34 residues that can be targeted in rational drug design approaches (Figure 7). While Pnt (SBi1) inhibited binding of p53 to S100B (*26*), it did not fully encompass the hydrophobic binding pocket identified in three S100B−peptide complexes determined at high resolution by NMR (S100B−$p53^{367-388}$, S100B−Ndr kinase, and S100B−TRTK12) (*50*, *59*, *60*), including residues in helix 2 (*36*), the hinge (residues 41 and 46−49), helix 3 (residues 51, 52, 55, 56, and 59), and helix 4 (residues 76, 79, 80, 82, and 86). Thus, identifying additional lead compounds that interact with these and other regions of S100B was pursued.

The structural studies here present three newly discovered lead molecules bound to Ca^{2+}-S100B (S100B−SBi132, S100B−SBi279, and S100B−SBi523). Using NMR and X-ray crystallography, the three compounds (SBi132, SBi279, and SBi523) were all found to bind the hydrophobic target binding pocket of Ca^{2+}-S100B at or near the $p53^{367-388}$, S100B−TRTK12, S100B−Ndr kinase, and/or S100B−Pnt binding sites (Figures 2−6); however, differences in the S100B binding sites for these three small molecules were discovered using both structural methods (Figures 2−6). For example, SBi279 and SBi523 both interacted with more residues in the hinge region than found in either of the Pnt−S100B complexes, but both of these compounds had fewer contacts with residues in helix 4 (Figure 7). SBi132 was the only compound that interacted with residues at the N-terminus of helix 4 (residues 76 and 79). On the other hand, several residues in the hinge (residues 42−45), helix 3 (residues 52, 55, and 56), and helix 4/C-terminal loop (residues 79, 83, 86, and 87) were involved in stabilizing several of the seven S100B−peptide or −SBi*X* complexes, so it is tempting to speculate that these particular residues are important for most S100B complexes, including that with full-length p53. Such "hot spots" in the Ca^{2+}-S100B binding site should be considered in future structure−activity relationship (SAR) and rational- and/or structure-based drug design strategies for effectively engineering S100B inhibitor (SBi*X*).

Of particular interest was the finding that SBi132 was found to bind Ca^{2+}-S100B specifically since no interaction was detected between SBi132 and Ca^{2+}-S100A1. Considering the high degree of sequence homology (56%, identical matches) between S100B and S100A1, there are differences in the binding region of SBi132 found on helix 4 (S100B, F76 and M79; S100A1, L77 and A80; alignment shifted by one residue) to allow for specificity. This result was in agreement with previous studies conducted by Arendt et al. (*61*), who discovered that several compounds they tested bound either S100B or S100A13, but in only a very few cases was a small molecule found to bind both S100 proteins. Even though S100B and S100A13 have a lower degree of sequence homology (22%, identical matches), these studies provide promise that the hydrophobic binding pockets in various S100 proteins (i.e., including S100B, S100A1, and S100A13) have unique features as to allow discovery of small molecules that can selectively bind one S100 protein or another. Lastly, the binding sites of SBi132, SBi279, and SBi523 represent new and previously undetected binding pockets and/or crevices in Ca^{2+}-S100B, sites that could be useful in the design of higher-affinity inhibitors that specifically block S100B.

SUMMARY

Three new S100B inhibitors (SBi132−, SBi279−, and SBi523−S100B) were found to bind Ca^{2+}-S100B using NMR approaches; however, the solution NMR data were not sufficient to precisely define the exact location and conformation of these SBi*X* molecules bound to Ca^{2+}-S100B. Therefore, high-quality crystals were obtained for each complex (SBi132−, SBi279−, and SBi523−S100B) and compared to those determined previously for Pnt−S100B and peptide−S100B complexes. Upon comparison, multiple small molecule binding sites on S100B were identified throughout the Ca^{2+}-S100B-exposed target protein binding pocket, including several hot spots that were involved in all of the complexes reported so far (Figure 7). Furthermore, identifying multiple small molecule binding sites using the available S100B−peptide and −SBi*X* structures will likely be important for future structure−activity relationship (SAR) studies and for medicinal chemistry strategies that target a single molecule that will bind one or more of these small molecule binding sites simultaneously. Such a molecule, which would potentially inhibit the S100B−p53 interaction at low concentrations (picomolar to nanomolar) in a specific fashion, could have therapeutic potential for treating malignant melanoma and other cancers with elevated levels of S100B.

ACKNOWLEDGMENT

We thank The University of Maryland Computer-aided Drug Design Center and The University of Maryland High Throughput Screening Core for their help in identifying small molecules that bind to S100B. We thank the staff of the 9-1 and 7-1 beamlines at the Stanford Synchrotron Radiation Lightsource for their assistance in collecting X-ray diffraction data.

REFERENCES

(1) Moore, B. (1965) A soluble protein characteristic of the nervous system. *Biochem. Biophys. Res. Commun. 19*, 739–744.
(2) Santamaria-Kisiel, L., Rintala-Dempsey, A. C., and Shaw, G. S. (2006) Calcium-dependent and -independent interactions of the S100 protein family. *Biochem. J. 396*, 201–214.
(3) Weber, D. J., Rustandi, R. R., Carrier, F., and Zimmer, D. B. (2000) Interaction of dimeric S100B($\beta\beta$) with the tumor suppressor protein: A model for Ca-dependent S100-target protein interactions , Kluwer Academic Publishers, Dordrecht, The Netherlands.
(4) Wilder, P. T., Varney, K. M., Weiss, M. B., Gitti, R. K., and Weber, D. J. (2005) Solution Structure of Zinc- and Calcium-Bound Rat

S100B as Determined by Nuclear Magnetic Resonance Spectroscopy. *Biochemistry 44*, 5690–5702.
(5) Deloulme, J. C., Assard, N., Mbele, G. O., Mangin, C., Kuwano, R., and Baudier, J. (2000) S100A6 and S100A11 are specific targets of the calcium- and zinc-binding S100B protein in vivo. *J. Biol. Chem. 275*, 35302–35310.
(6) Barber, K. R., McClintock, K. A., Jamieson, G. A., Dimlich, R. V., and Shaw, G. S. (1999) Specificity and Zn^{2+} enhancement of the S100B binding epitope TRTK-12. *J. Biol. Chem. 274*, 1502–1508.
(7) Baudier, J., and Cole, R. D. (1988) Interactions between the microtubule-associated tau proteins and S100b regulate tau phosphorylation by the Ca^{2+}/calmodulin-dependent protein kinase II. *J. Biol. Chem. 263*, 5876–5883.
(8) Gentil, B. J., Delphin, C., Mbele, G. O., Deloulme, J. C., Ferro, M., Garin, J., and Baudier, J. (2001) The giant protein AHNAK is a specific target for the calcium- and zinc-binding S100B protein: Potential implications for Ca^{2+} homeostasis regulation by S100B. *J. Biol. Chem. 276*, 23253–23261.
(9) Zimmer, D. B., Cornwall, E. H., Landar, A., and Song, W. (1995) The S100 protein family: History, function, and expression. *Brain Res. Bull. 37*, 417–429.
(10) Donato, R. (2003) Intracellular and extracellular roles of S100 proteins. *Microsc. Res. Tech. 60*, 540–551.
(11) Heizmann, C. W. (2002) The multifunctional S100 protein family. *Methods Mol. Biol. 172*, 69–80.
(12) Hansson, L. O., Vonschoultz, E., Djureen, E., Hansson, J., Nilsson, B., and Ringborg, U. (1997) Prognastic value of serum analyses of S100 protein β in malignant melanoma. *Anticancer Res. 17*, 3071–3073.
(13) Maelandsmo, G. M., Florenes, V. A., Mellingsaeter, T., Hovig, E., Kerbel, R. S., and Fodstad, O. (1997) Differential expression patterns of S100A2, S100A4 and S100A6 during progression of human malignant melanoma. *Int. J. Cancer 74*, 464–469.
(14) Boni, R., Heizmann, C. W., Doguoglu, A., Ilg, E. C., Schafer, B. W., Dummer, R., and Burg, G. (1997) Ca^{2+}-binding proteins S100A6 and S100B in primary cutaneous melanoma. *J. Cutaneous Pathol. 24*, 76–80.
(15) Camby, I., Lefranc, F., Titeca, G., Neuci, S., Fastrez, M., Dedecken, L., Schafer, B. W., Brotchi, J., Heizmann, C. W., Pochet, R., Salmon, I., Kiss, R., and Decaestecker, C. (2000) Differential expression of S100 calcium-binding proteins characterizes distinct clinical entities in both WHO grade II and III astrocytic tumours. *Neuropathol. Appl. Neurobiol. 26*, 76–90.
(16) Camby, I., Nagy, N., Lopes, M. B., Schafer, B. W., Maurage, C. A., Ruchoux, M. M., Murmann, P., Pochet, R., Heizmann, C. W., Brotchi, J., Salmon, I., Kiss, R., and Decaestecker, C. (1999) Supratentorial pilocytic astrocytomas, astrocytomas, anaplastic astrocytomas and glioblastomas are characterized by a differential expression of S100 proteins. *Brain Pathol. 9*, 1–19.
(17) Davey, G. E., Murmann, P., and Heizmann, C. W. (2001) Intracellular Ca^{2+} and Zn^{2+} levels regulate the alternative cell density-dependent secretion of S100B in human glioblastoma cells. *J. Biol. Chem. 276*, 30819–30826.
(18) Hauschild, A., Engel, G., Brenner, W., Glaser, R., Monig, H., Henze, E., and Christophers, E. (1999) Predictive value of serum S100B for monitoring patients with metastatic melanoma during chemotherapy and/or immunotherapy. *Br. J. Dermatol. 140*, 1065–1071.
(19) Hauschild, A., Engel, G., Brenner, W., Glaser, R., Monig, H., Henze, E., and Christophers, E. (1999) S100B protein detection in serum is a significant prognostic factor in metastatic melanoma. *Oncology 56*, 338–344.
(20) Hauschild, A., Michaelsen, J., Brenner, W., Rudolph, P., Glaser, R., Henze, E., and Christophers, E. (1999) Prognostic significance of serum S100B detection compared with routine blood parameters in advanced metastatic melanoma patients. *Melanoma Res. 9*, 155–161.
(21) Baudier, J., Delphin, C., Grunwald, D., Khochbin, S., and Lawrence, J. J. (1992) Characterization of the tumor suppressor protein p53 as a protein kinase C substrate and a S100b-binding protein. *Proc. Natl. Acad. Sci. U.S.A. 89*, 11627–11631.
(22) Rustandi, R. R., Baldisseri, D. M., and Weber, D. J. (2000) Structure of the negative regulatory domain of p53 bound to S100B. *Nat. Struct. Biol. 7*, 570–574.
(23) Rustandi, R. R., Drohat, A. C., Baldisseri, D. M., Wilder, P. T., and Weber, D. J. (1998) The Ca^{2+}-dependent interaction of S100B with a peptide derived from p53. *Biochemistry 37*, 1951–1960.
(24) Delphin, C., Ronjat, M., Deloulme, J. C., Garin, G., Debussche, L., Higashimoto, Y., Sakaguchi, K., and Baudier, J. (1999) Calcium-dependent interaction of S100B with the C-terminal domain of the tumor suppressor p53. *J. Biol. Chem. 274*, 10539–10544.
(25) Lin, J., Yang, Q., Yan, Z., Markowitz, J., Wilder, P. T., Carrier, F., and Weber, D. J. (2004) Inhibiting S100B restores p53 levels in primary malignant melanoma cancer cells. *J. Biol. Chem. 279*, 34071–34077.
(26) Wilder, P. T., Lin, J., Bair, C. L., Charpentier, T. H., Yang, D., Liriano, M., Varney, K. M., Lee, A., Oppenheim, A. B., Adhya, S., Carrier, F., and Weber, D. J. (2006) Recognition of the tumor suppressor protein p53 and other protein targets by the calcium-binding protein S100B. *Biochim. Biophys. Acta,* 1284–1297.
(27) Markowitz, J., Chen, I., Gitti, R., Baldisseri, D. M., Pan, Y., Udan, R., Carrier, F., MacKerell, A. D., and Weber, D. J. (2004) Identification and characterization of small molecule inhibitors of the calcium-dependent S100B-p53 tumor suppressor interaction. *J. Med. Chem. 47*, 5085–5093.
(28) Markowitz, J., Mackerell, A. D., Carrier, F., Charpentier, T. H., and Weber, D. J. (2005) Design of Inhibitors for S100B. *Curr. Top. Med. Chem. 5*, 1093–1108.
(29) Markowitz, J., MacKerell, A. D., and Weber, D. J. (2007) A search for inhibitors of S100B, a member of the S100 family of calcium-binding proteins. *Mini Rev. Med. Chem. 7*, 609–616.
(30) Charpentier, T. H., Wilder, P. T., Liriano, M. A., Varney, K. M., Pozharski, E., MacKerell, A. D., Coop, A., Toth, E. A., and Weber, D. J. (2008) Divalent metal ion complexes of S100B in the absence and presence of pentamidine. *J. Mol. Biol. 382*, 56–73.
(31) Drohat, A. C., Baldisseri, D. M., Rustandi, R. R., and Weber, D. J. (1998) Solution structure of calcium-bound rat S100B as determined by nuclear magnetic resonance spectroscopy. *Biochemistry 37*, 2729–2740.
(32) Mori, S., Abeygunawardana, C., Johnson, M. O., and van Zijl, P. C. (1995) Improved sensitivity of HSQC spectra of exchanging protons at short interscan delays using a new fast HSQC (FHSQC) detection scheme that avoids water saturation. *J. Magn. Reson., Ser. B 108*, 94–98.
(33) Kay, L. E., Keifer, P., and Saarinen, T. (1992) Pure absorption gradient enhanced heteronuclear single quantum correlation spectroscopy with improved sensitivity. *J. Am. Chem. Soc. 114*, 10663–10665.
(34) Delaglio, F., Grzesiek, S., Vuister, G. W., Zhu, G., Pfeifer, J., and Bax, A. (1995) NMRPipe: A multidimensional spectral processing system based on UNIX pipes. *J. Biomol. NMR 6*, 277–293.
(35) Edison, A. S., Abildgaard, F., Westler, W. M., Mooberry, E. S., and Markley, J. L. (1994) Practical introduction to theory and implementation of multinuclear, multidimensional nuclear magnetic resonance experiments. *Methods Enzymol. 239*, 3–79.
(36) Live, D. H., Davis, D. G., Agosta, W. C., and Cowburn, D. (1984) Longe range hydrogen bond mediated effects in peptides: ^{15}N NMR study of gramicidin S in water and organic solvents. *J. Am. Chem. Soc. 106*, 1939–1941.
(37) Spera, S., and Bax, A. (1991) Empirical correlation between protein backbone conformation and Cα and Cβ/13-C nuclear magnetic resonance chemical shifts. *J. Am. Chem. Soc. 113*, 5490–5492.
(38) Mayer, M., and Meyer, B. (2001) Group epitope mapping by saturation transfer difference NMR to identify segments of a ligand in direct contact with a protein receptor. *J. Am. Chem. Soc. 123*, 6108–6117.
(39) Bax, A., and Davis, D. G. (1985) Practical aspects of two-dimensional transverse NOE spectroscopy. *J. Magn. Reson. 63*, 207–213.
(40) Otwinowski, Z., and Minor, W. (1997) Processing of X-ray diffraction data collected in oscillation mode. *Methods Enzymol. 276*, 307–326.
(41) Matsumura, H., Shiba, T., Inoue, T., Harada, S., and Kai, Y. (1998) A novel mode of target recognition suggested by the 2.0 Å structure of holo S100B from bovine brain. *Structure 6*, 233–241.
(42) Vagin, A. A., and Isupov, M. N. (2001) Spherically averaged phased translation function and its application to the search for molecules and fragments in electron-density maps. *Acta Crystallogr. D57*, 1451–1456.
(43) Murshudov, G. N., Vagin, A. A., and Dodson, E. J. (1997) Refinement of macromolecular structures by the maximum-likelihood method. *Acta Crystallogr. D53*, 240–255.
(44) Emsley, P., and Cowtan, K. (2004) Coot: Model-building tools for molecular graphics. *Acta Crystallogr. D60*, 2126–2132.
(45) Laskowski, R. A., MacArthur, M. W., Moss, D. S., and Thornton, J. M. (1993) PROCHECK: A program to check the stereochemical quality of protein structures. *J. Appl. Crystallogr. 26*, 283–291.
(46) Laskowski, R. A., MacArthur, M. W., and Thornton, J. M. (1998) Validation of protein models derived from experiment. *Curr. Opin. Struct. Biol. 8*, 631–639.

(47) Berman, H. M., Westbrook, J., Feng, Z., Gilliland, G., Bhat, T. N., Weissig, H., Shindyalov, I. N., and Bourne, P. E. (2000) The Protein Data Bank. *Nucleic Acids Res. 28*, 235–242.
(48) Yang, H., Guranovic, V., Dutta, S., Feng, Z., Berman, H. M., and Westbrook, J. D. (2004) Automated and accurate deposition of structures solved by X-ray diffraction to the Protein Data Bank. *Acta Crystallogr. D60*, 1833–1839.
(49) Lin, J., Blake, M., Tang, C., Zimmer, D., Rustandi, R. R., Weber, D. J., and Carrier, F. (2001) Inhibition of p53 transcriptional activity by the S100B calcium-binding protein. *J. Biol. Chem. 276*, 35037–35041.
(50) Rustandi, R. R., Baldisseri, D. M., Drohat, A. C., and Weber, D. J. (1999) Structural changes in the C-terminus of Ca^{2+}-bound rat S100B($\beta\beta$) upon binding to a peptide derived from the C-terminal regulatory domain of p53. *Protein Sci. 8*, 1743–1751.
(51) Yan, J., Kline, A. D., Mo, H., Shapiro, M. J., and Zartler, E. R. (2003) The effect of relaxation on the epitope mapping by saturation transfer difference NMR. *J. Magn. Reson. 163*, 270–276.
(52) Baudier, J., Glasser, N., and Gerard, D. (1986) Ions binding to S100 proteins. I. Calcium- and zinc-binding properties of bovine brain S100$\alpha\alpha$, S100a($\alpha\beta$), and S100b($\beta\beta$) protein: Zn^{2+} regulates Ca^{2+} binding on S100b protein. *J. Biol. Chem. 261*, 8192–8203.
(53) Kligman, D., and Hilt, D. C. (1988) The S100 protein family. *Trends Biochem. Sci. 13*, 437–443.
(54) Strynadka, N. C., and James, M. N. (1989) Crystal structures of the helix-loop-helix calcium-binding proteins. *Annu. Rev. Biochem. 58*, 951–998.
(55) Amburgey, J. C., Abildgaard, F., Starich, M. R., Shah, S., Hilt, D. C., and Weber, D. J. (1995) ^{1}H, ^{13}C and ^{15}N NMR assignments and solution secondary structure of rat Apo-S100β. *J. Biomol. NMR 6*, 171–179.
(56) Drohat, A. C., Amburgey, J. C., Abildgaard, F., Starich, M. R., Baldisseri, D., and Weber, D. J. (1996) Solution structure of rat apo-S100B as determined by NMR spectroscopy. *Biochemistry 35*, 11577–11588.
(57) Zhong, S., Macias, A. T., and MacKerell, A. D. (2007) Computational identification of inhibitors of protein-protein interactions. *Curr. Top. Med. Chem. 7*, 63–82.
(58) Ostendorp, T., Leclerc, E., Galichet, A., Koch, M., Demling, N., Weigle, B., Heizmann, C. W., Kroneck, P. M., and Fritz, G. (2007) Structural and functional insights into RAGE activation by multimeric S100B. *EMBO J. 26*, 3868–3878.
(59) Inman, K. G., Yang, R., Rustandi, R. R., Miller, K. E., Baldisseri, D. M., and Weber, D. J. (2002) Solution NMR structure of S100B bound to the high-affinity target peptide TRTK-12. *J. Mol. Biol. 324*, 1003–1014.
(60) Bhattacharya, S., Large, E., Heizmann, C. W., Hemmings, B., and Chazin, W. J. (2003) Structure of the Ca^{2+}/S100B/NDR kinase peptide complex: Insights into S100 target specificity and activation of the kinase. *Biochemistry 42*, 14416–14426.
(61) Arendt, Y., Bhaumik, A., Del Conte, R., Luchinat, C., Mori, M., and Porcu, M. (2007) Fragment Docking to S100 Proteins Reveals a Wide Diversity of Weak Interaction Sites. *ChemMedChem 2*, 1648–1654.